



Towards Efficient Information Fusion: Concentric Dual Fusion Attention Based Multiple Instance Learning for Whole Slide Images

Yujian Liu¹ ^{*}, Ruoxuan Wu¹ ^{*}, Xinjie Shen^{1*} , Zihuang Lu¹, Lingyu Liang¹ [†], Haiyu Zhou², Shipu Xu³, Shaoai Cai⁴, and Shidang Xu¹ [†]

¹ South China University of Technology, Guangzhou, China

² Guangdong Provincial People's Hospital, Guangzhou, China

³ Sun Yat-sen University, Guangzhou, China

⁴ The Second affiliated hospital of Guangzhou Medical University, Guangzhou, China

Abstract. In the realm of digital pathology, multi-magnification Multiple Instance Learning (multi-mag MIL) has proven effective in leveraging the hierarchical structure of Whole Slide Images (WSIs) to reduce information loss and redundant data. However, current methods fall short in bridging the domain gap between pretrained models and medical imaging, and often fail to account for spatial relationships across different magnifications. Addressing these challenges, we introduce the Concentric Dual Fusion Attention-MIL (CDFA-MIL) framework, which innovatively combines point-to-area feature-column attention and point-to-point concentric-row attention using concentric patch. This approach is designed to effectively fuse correlated information, enhancing feature representation and providing stronger correlation guidance for WSI analysis. CDFA-MIL distinguishes itself by offering a robust fusion strategy that leads to superior WSI recognition. Its application has demonstrated exceptional performance, significantly surpassing existing MIL methods in accuracy and F1 scores on prominent datasets like Camelyon16 and TCGA-NSCLC. Specifically, CDFA-MIL achieved an average accuracy and F1-score of 93.7% and 94.1% respectively on these datasets, marking a notable advancement over traditional MIL approaches.

Keywords: Whole Slide Images · Reduced Field Gap · Attention Mechanism · Correlation

1 Introduction

Histopathological whole slide images (WSIs) analysis, crucial for cancer diagnostics and therapy assessment, grapples with vast image scales and limitations in traditional feature extraction [13, 18, 43]. Deep learning advancements, including patch-based CNNs [9], WSIAS [46], and CLAM [20], while promising, struggle with the immense size of WSIs (about $40,000 \times 40,000$ pixels), challenging their

^{*} Equal contribution. [†]Correspondence: lianglysky@gmail.com, xushidang@gmail.com

computational efficiency [2, 14, 34, 44]. Efforts to manage these challenges, such as low-resolution input via manual region of interest (ROIs) annotation [4, 22] and unsupervised clustering [23, 46] or selective patch sampling [13, 16], often face labor intensity and uncertainty errors affecting recognition accuracy. Consequently, developing methodologies that enable deep learning models to efficiently process WSIs, with their millions of pixels, is pivotal for advancing digital pathology.

Multiple Instance Learning (MIL) has become instrumental in accurately recognizing WSIs under weak supervision [2, 3, 12, 14, 20, 21]. In MIL, WSIs are divided into myriad diminutive patches, which subsequently undergo processing via a feature extractor and classifier — commonly a Convolutional Neural Network paired with a Multilayer Perceptron. This approach brings two main advantages: it allows for the effective extraction of high-resolution features by dividing the WSIs [6] and offers a comprehensive feature overview, bypassing the limitations of targeting only specific areas or superficial features [2, 20, 42]. However, challenges arise in the division of patches and their subsequent aggregation. The formulaic approach of patch division may inadvertently truncate morphological details, as patches operate independently, potentially segmenting single cells or tissues across multiple patches [3, 32]. Due to an excess of patches unrelated to diagnosis, irrelevant information floods into the feature aggregation stage [36, 44]. Multi-magnification MIL (multi-mag MIL) addresses these issues by incorporating magnifications containing both fine- and coarse-grained information present in WSIs, providing enhanced information preservation [31, 34] and alignment with medical diagnostic practices [3, 17] (Fig. 1). This approach outperforms single-magnification techniques, providing a more detailed and clinically relevant analysis of pathology.

While multi-mag MIL has shown promise in cancer diagnostics and prognosis [7, 10, 14, 39], the optimization of fusion processes across different magnifications remains a critical and relatively unexplored area [26]. Due to differences in morphological representations, merging data from multiple magnifications poses challenges. Patch features extracted by a pre-trained model with domain gap, or fusing patches from distant and weakly presented areas, can significantly impair the model’s discriminative power [5, 14, 15, 30, 34, 38, 40]. Specifically, the major challenges in fusion across magnifications are:

- **Domain Gap in Feature Encoding:** Enhancing the feature representation capability of pre-trained models is crucial, especially considering the domain gap in feature encoding. Pre-trained models might not be inherently equipped to handle the nuances of pathology images at varying magnifications.
- **Need for Precise Spatial Correlations:** Global fusion methods, influenced by the inclusion of numerous distant patches in feature aggregation, often neglect the crucial spatial relationships between magnifications. Establishing a method that accurately captures and utilizes spatial correlations across magnifications is essential but remains an unresolved challenge.

- Lack of well-formulated concentric patch approach: There is a need for a more systematic and robust approach to utilize concentric patch, which could ensure better utilization of available data.

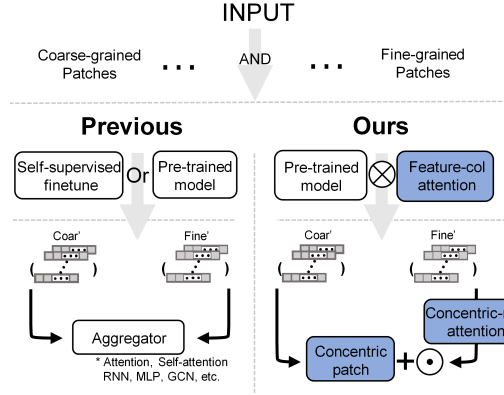


Fig. 1: An illustration of the difference between previous-MIL and our CDFA-MIL framework: Despite the use of varying magnifications, traditional MIL approaches merely extract and aggregate patch features through simple aggregators. In contrast, our method initially refines the feature representations extracted by a pre-trained model via a feature-column attention mechanism. Subsequently, it combines both coarse and fine-grained features through dot-multiplication, leveraging the point-to-point relationship of concentric patch and a concentric-row attention mechanism.

Our innovative Concentric Dual Fusion Attention-MIL (CDFA-MIL) framework (Fig. 2), rooted in classical attention concepts [11, 12, 20, 32, 34, 39] and pathologists’ diagnostic processes, significantly advances the field of feature fusion in pathology image analysis. This novel approach effectively overcomes the constraints of pre-trained models and the challenges posed by large patch datasets. Key contributions of CDFA-MIL include:

- **Point-to-Area Feature Enhancement Method:** This method utilizes a point-to-area feature-column attention mechanism of channel correlation modeling to assign weights for each patch’s feature, enhancing the feature representation ability without the need for self-supervised pretext task training. It demonstrates substantial improvements in information entropy and T-SNE feature visualization, as validated by ablation experiments.
- **Point-to-Point Precise Spatial Fusion Strategy:** CDFA-MIL employs a point-to-point concentric-row attention mechanism, efficiently managing the influence of distant patches in fusion. This strategy involves mapping relationships between different magnifications, utilizing coordinate transformations, and overlapping techniques. It focuses on assessing the surroundings

of known abnormal areas, particularly after detecting anomalies at higher resolutions.

- **Enhanced Performance in Cancer Subtype Classification:** Applied to multi-cancer subtype classification, CDFA-MIL demonstrates superior performance over traditional MIL methods. It achieves remarkable accuracy and AUC scores in prominent datasets like Camelyon-16 and TCGA-NSCLC.

Overall, CDFA-MIL stands out as a cutting-edge framework, addressing crucial gaps in feature representation and fusion in digital pathology, and setting a new benchmark in the field.

2 Related work

2.1 Multiple Instance Learning for Analysis

Since 1997, Multiple Instance Learning (MIL) has advanced significantly, influencing domains from computer vision to bioinformatics [18, 21, 45]. In WSI cancer detection, MIL classifies a slide based on the presence (positive) or absence (negative) of cancer. MIL operates at instance [2, 9] and bag levels [12, 14, 15, 24, 29], with the latter preferred for its accuracy and avoiding cancerous regions' sparsity in WSIs, leading to labeling noise [44].

Bag-level MIL often faces a domain gap when using non-medical pre-trained models, affecting feature representation [5, 14, 15, 30, 38, 40]. While self-supervised learning has attempted to address this, it confronts WSI's inherent imbalance and training costs caused by the huge number of patches [25, 33]. This study introduces a channel attention mechanism, specifically point-to-area columnar focus, enhancing patch feature saliency and instance representation in bag-level MIL without extensive secondary pretext task training [11].

2.2 Pyramid Structure Images in Histopathology

WSIs' cellular and tissue diversity complicates single-magnification MIL, as low magnification can miss crucial details and high magnification may neglect context [3, 32, 34]. Multi-mag MIL, enhancing morphological insight by incrementally revealing multiscale features [3, 7, 10, 26, 39], overcomes this. However, traditional methods that globally fuse features from different magnifications often neglect spatial correlations and inadvertently incorporating distant patches, thus reducing precision (Fig. 4).

Point-to-point fusion with concentric patches [28, 37] addresses this by focusing on correlated patches but can result in substantial pixel-level information loss at high magnification, a crucial gap needing improvement in current concentric patch techniques (Fig. 3 (B)).

2.3 MIL with Attention Mechanism

Inspired by the human visual system, attention mechanisms have been developed to mimic the way humans process visual information by prioritizing the salient and significant areas and features within an image [27]. However, recognizing the significant areas and features within an entire WSI with millions of pixels is a formidable task [2, 42].

Attention mechanisms, inspired by human visual processing, prioritize key image areas and features [27]. Identifying these within WSIs, which contain millions of pixels, poses significant challenges [2, 42]. Attention-Based MIL [12] excels by using attention scores from instance representations to construct weighted slide representations. This has led to several MIL approaches [20, 29, 34, 39, 40], including CLAM [20] which scores patches and combines attention scores and features. Zoom-MIL [34] employs a hierarchical approach, initially using attention at lower magnifications for ROI selection, then examining in greater detail at higher magnifications. The advanced HIPT framework [3] utilizes a self-supervised, hierarchical self-attention method from cellular to regional levels, addressing information sparsity at multiple magnifications.

3 Method

3.1 MIL for WSIs Analysis

Dividing Patch. Given a WSI X , the goal is to make slide-level prediction Y by learning a classifier $f(X; \theta)$. Due to its high resolution, X is divided into an extensive set of small instances (patches) denoted as $X = \{x_1, x_2, \dots, x_N\}$, where N represents the total number of instances. Each instance can be regarded as a localized image with unique spatial positioning and distinctive features.

Feature Encoding. In the case of each individual instance, it is customary to employ pre-trained model such as those from ImageNet [6] to acquire feature representations. However, in scenarios characterized by slide-level supervised labels \tilde{Y} , the labels \tilde{y}_i for each instance are usually unknown, rendering fine-tuning of pre-trained model challenging.

$$F = \{f(x_i; \theta_1) | i \in \{1, 2, \dots, N\}\} \quad (1)$$

the symbol f represents the function with parameter θ_1 for feature extraction from instances, such as ResNet [8] or Vision Transformer [19], while F represents the numerous instance feature set.

Features Aggregation and Classification. The features from all instances within the set F are aggregated to form slide-level encoded features, and then generate slide-level predictions \tilde{Y} by a multi-layer perceptron (MLP).

$$\tilde{Y} = \text{argmax}(\text{MLP}(g(F; \theta_2); \theta_3)) \quad (2)$$

g is an aggregation operator with parameter θ_2 that combine instance features and then feeds them into an MLP classifier with parameter θ_3 to predict \tilde{Y} . The argmax function returns the index at which the maximum value is located.

3.2 Concentric Dual Fusion Attention-MIL (CDFA-MIL) for WSIs Analysis

We propose a novel CDFA-MIL framework for analysis of WSIs, which is illustrated in Fig. 2. We first divide high magnification (such as $40\times$) WSIs into patches to obtain fine-grained information. Based on these divisions, we subdivide WSIs at low or medium magnifications (such as $10\times$ or $20\times$) in a concentric manner to obtain point-to-point coarse-grained information. The generated concentric patches with uniform size and amount are put into a concentric dual fusion attention block to enhance their representational capability and extract compact and discriminate features. Finally, we utilize a classifier to identify slide-level predictions by analyzing features aggregated from multiple patches and fused at different magnification levels. In the following subsections, we will provide detailed explanations of the division of concentric patch, the design of the concentric dual fusion attention, and the learning strategies for the entire framework.

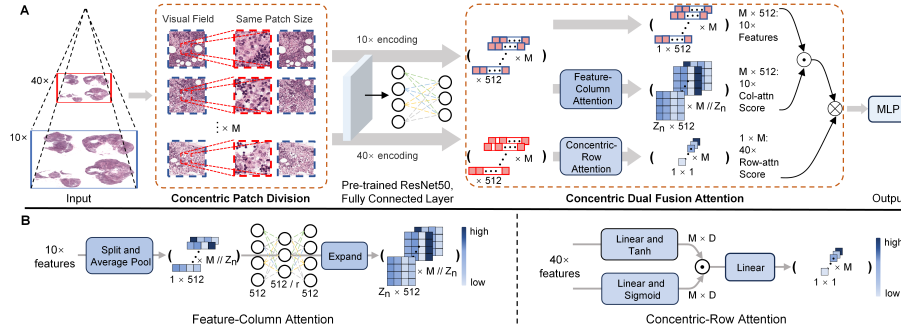


Fig. 2: Workflow of the CDFA-MIL framework: A) High-magnification ($40\times$) patches are scaled to lower magnifications ($10\times$) for feature extraction using pre-trained ResNet-50 [8]. CDFA-MIL utilizes dual fusion attention, combining feature-column and concentric-row attentions, to merge features across magnifications for MLP classification. B) The dual fusion attention mechanism intricately combines feature-column and concentric-row attentions.

Divide Concentric Patch. In clinical practice, pathologists adopt a hierarchical observation approach. In electron microscopy for WSI, the objective and eyepiece sizes are typically fixed, maintaining a constant field of view. Observation of the entire tissue section is achieved by adjusting the focal length for magnification and moving the slide to navigate the area of interest. Initially, they conduct a comprehensive examination of tissue-level information from low-resolution WSIs, focusing on structures like vascular patterns and glandular arrangements. They proceed to diagnose cellular-level details by increasing the magnification of WSIs after suspecting abnormal regions, such as nuclear morphology and microenvironment. Upon discovering cellular-level abnormal area,

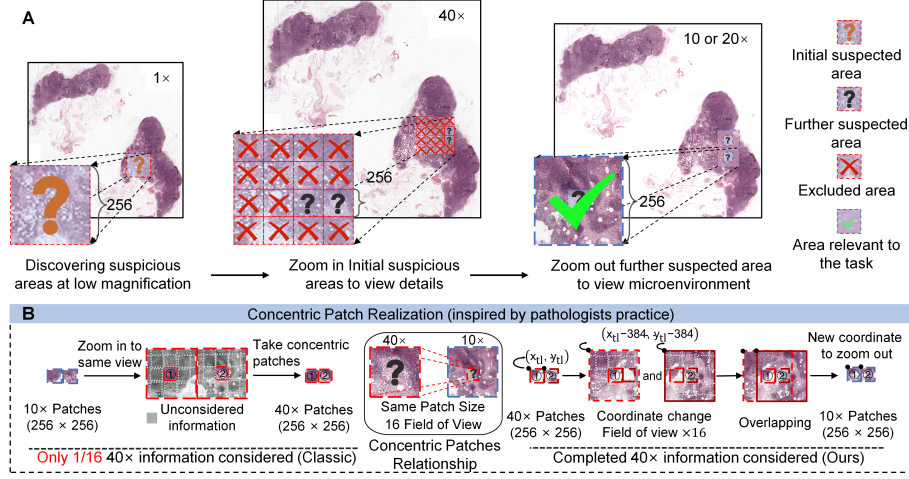


Fig. 3: Concentric patch inspiration and technical improvements: A) The general diagnostic process of pathologists for WSIs recognition: Pathologists, when examining pathological images, typically begin their inspection by identifying abnormal areas at lower magnification. Subsequently, they increase the resolution (magnification) for further investigation. Upon identifying abnormal cells or tissues, they lower the magnification to focus on the specific area of interest, assessing the surrounding region (concentric patch) for any abnormalities. B) Comparison of concentric patch realization methods. Our optimized solution utilized 40× and corresponding coordinate transformed and overlapped 10× patches. It consider more completed 40× information than previous method, which loss $\frac{15}{16}$ fine grain information.

pathologists reduce the magnification to observe its surrounding tissue in greater detail for further evaluation (Fig. 3 (A)). To simulate this diagnostic process, we divided concentric patches with same size but different fields of view based on the spatial pyramid structure of WSIs for strongly correlated areas fusion.

The CLAM toolbox [20] was applied for patch division. Initially, a patch size of 256×256 and a step size of 256 were set under high magnification to obtain cellular-level information. The coordinates of the patches top-left corner were recorded as (x_{tl}, y_{tl}) . To create patches with 4^2 times the information while maintaining the same center and pixel count, a line was extended from the patch's center to its upper-left corner, making it four times longer. This generates a new left top point $(x_{tl} - 384, y_{tl} - 384)$, and we set 256×256 patch size under patch level N_{low} (down-sampling varies for different WSIs). By keeping the step size at 256, low magnification patches with the same number and pixel count as the high magnification patches were obtained, as shown in Fig. 3 (B). Similarly, the top-left coordinates were adjusted to $(x_{tl} - 128, y_{tl} - 128)$, the patch level was set to N_{med} , and the other parameters remained unchanged to obtain patches under medium magnification.

Enhancing Patch Representation. Propagating gradients across a large number of patches poses challenges. Typical approaches involves mapping each patch x_i to a feature vector $h_i = f(x_i; \theta_1) \in R^{1 \times M}$ through a pre-trained model f , and then concatenating these vectors to form a slide-level representation. However, pre-trained model are usually trained on natural images and may not readily adapt to medical image features, leading to weak patch representations. Additionally, it is hard to fine-tune the pre-trained model because patches' label \tilde{y}_i are unknown. Self-supervision, on the other hand, utilizes the pretext task to fine-tune the model, but faces the inherent imbalance of WSIs and the cost of training due to the large number of patches. In this section, we draw inspiration from the squeeze-and-excitation principle [11] to improve the above issues without the need for expensive secondary training, as shown in the pseudo code of supplementary materials.

For slide features at low magnification SF_l , represented as:

$$SF_l = \text{concatenate}(\{PF_l^i, PF_l^i \in R^{1 \times M} | i \in \{1, 2, \dots, N\}\}) \quad (3)$$

where PF_l^i denotes the patch features at low magnification for the i th patch, N is the number of patches, and M is the dimension of the features. To start, we divide the surrounding regions $SR(j)$ for each patch:

$$SR(j) = \begin{cases} sr & \text{if } j \leq \frac{N}{sr} - 1 \\ N \bmod sr & \text{if } j = \frac{N}{sr} \text{ and } N \bmod sr \neq 0 \end{cases} \quad (4)$$

sr is a hyperparameter, and we set it to 512 to represent the number of surrounding patches taken into account. $N \bmod sr$ represents the remainder when the number of patches is not divisible by sr .

Then, we generate $Avg(j)$ for M scalar values by averaging the distribution information over each dimension space m_i of $RS(j) \times M$, where each scalar represents the global importance description of the corresponding feature point to a $RS(j)$ area:

$$Avg(j) = \{\frac{1}{RS(j)} \sum_{RS(j)} m_i | i \in \{1, 2, \dots, M\}\} \quad (5)$$

Furthermore, inspired by the Excitation principle, we employ fully connected layers to learn how to redistribute the significant weights for each feature point, obtaining channel-level dependencies:

$$CSL(j) = \text{softmax}(\sigma(\delta(Avg(j)W_1)W_2)) \quad (6)$$

$$CS_l = \text{concatenate}(\{CSL(j) | j \in 1, 2, \dots, \frac{N}{sr}\}) \quad (7)$$

Among them, $CSL(j)$ represents the feature-column attention scores in a certain $SR(j)$ area, and $CS_l \in R^{N \times M}$ represents the feature-column attention scores of all patches at low magnification. The δ and σ represent the ReLU and Sigmoid

activation functions, respectively. $W_1 \in R^{M \times \frac{M}{r}}$ and $W_2 \in R^{\frac{M}{r} \times M}$, where r is a scaling factor primarily used to reduce network computational complexity and the number of parameters. The term concatenate is used to combine attention scores from multiple areas.

Finally, CS_l is pointwise multiplied with SF_l to enhance the patch feature representation:

$$\tilde{SF}_l = CS_l \odot SF_l \quad (8)$$

Weighting the Significance of Patches. In the context of disease diagnosis using WSIs, the contribution of each patch varies. Therefore, patches should be assigned different scores, allowing representative patches to receive higher scores. In the previous section, we addressed weak representation through feature-column attention. In this section, we measure the significance of patches through point-to-point concentric-row attention.

For slide features at high magnification SF_h , represented as:

$$SF_h = \text{concatenate}(\{PF_h^i, PF_h^i \in R^{1 \times M} | i \in \{1, 2, \dots, N\}\}) \quad (9)$$

where PF_h^i denotes the patch features at high magnification for the i th patch, N is the number of patches, and M is the dimension of the features. Similarly, for enhanced slide features at low magnification, there exists $\tilde{SF}_l = \text{concatenate}(\{PF_l^i, \tilde{PF}_l^i \in R^{1 \times M} | i \in \{1, 2, \dots, N\}\})$. To avoid performing long-distance global fusion with multiple magnifications patches (Fig. 4), we used a concentric patch division method, so for each PF_h^i , there will always be a unique concentric \tilde{PF}_l^i , and its corresponding relationship is shown in Fig. 3 (B). We use Gated Attention for each PF_h^i Perform attention rating:

$$a_i = \frac{\exp \{W^\top (\tanh(VF_i) \odot \eta(UF_i))\}}{\sum_{j=1}^N \exp \{W^\top (\tanh(VF_j) \odot \eta(UF_j))\}} \quad (10)$$

where F_i is patch features PF_h^i , $W \in R^{L \times 1}$, $V \in R^{L \times D}$ and $U \in R^{L \times D}$ are learnable parameters with hidden dimension L , \odot is element-wise multiplication, and η is the sigmoid function. subsequently, a weighted method is utilized to assess the significance of \tilde{PF}_l^i :

$$\tilde{Y} = \text{argmax}(\text{MLP}(\sum_i^N a_i \tilde{PF}_l^i)) \quad (11)$$

a_i represents the attention scores of high magnification-level patches to weight the significance of PF_h^i . \tilde{PF}_l^i corresponds to the features of a_i -associated concentric patch. \tilde{Y} represents the predicted result. This operation aligns with the procedure of reducing the zoom level to observe the surroundings when high magnification-level abnormal areas are already identified.

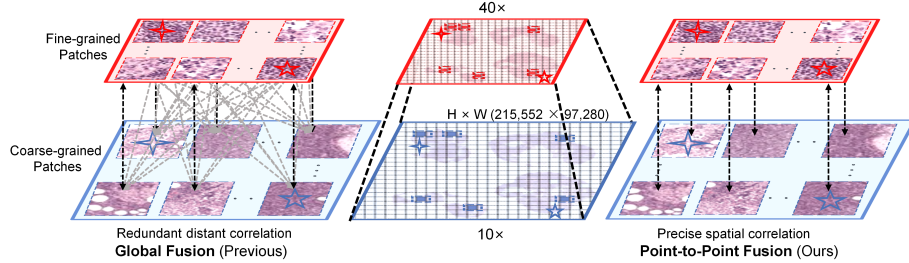


Fig. 4: Comparison of 40 \times and 10 \times multi-magnification fusion methods: Global fusion overlooks spatial correlations across varying magnifications, often merging distant, weakly related patches, thereby creating redundancy. Our point-to-point fusion method, in contrast, leverages direct relationships within concentric patches for accurate, robustly correlated spatial integration.

4 Experiments

In this section, we present the performance of the CDFA-MIL framework and compare it with current state-of-the-art classification frameworks on two real-world datasets. Additionally, Ablation experiments are performed to further study the proposed method.

4.1 Experimental Setup

Datasets Description. We assess our method’s slide-level classification efficacy against current top-tier algorithms using two public histopathology WSIs datasets: Camelyon-16 [1], focusing on binary tumor/normal classification, and The Cancer Genome Atlas Non-Small Cell Lung Cancer (TCGA-NSCLC) [35] for tumor subtyping.

CAMELYON-16 dataset has 160 normal tissue WSIs and 110 tumor tissue in its training set, and 129 slides in test set. Notably, some slides feature minuscule tumor lesions, challenging detection accuracy. We only use slide-level labels for implementation, disregarding annotations provided at patch level by pathologists.

TCGA-NSCLC dataset consists of two subdivisions: lung adenocarcinoma (TCGA-LUAD) and lung squamous cell carcinoma (TCGA-LUSC), comprising a total of 1053 diagnostic WSIs - 541 LUAD from 478 cases and 512 LUSC from an equal number of cases.

Implementation Details. For evaluation, we employed three metrics for binary classification: accuracy (ACC), F1-score (F1), and area under the curve (AUC). In pre-processing, we divided patches and extracted their features following CLAM-SB protocols [20]. This including extracting non-overlapping patches of 256×256 under high magnification, and using the same dimensions with overlap in tissue areas under lower magnification. The average patch count per slide at 20 \times magnification is approximately 45,726 for Camelyon-16 and 3,084

for TCGA-NSCLC datasets. Feature encoding employs ResNet-50 model, pre-trained on the ImageNet-1K dataset.

Experimentally, the Camelyon-16 dataset’s 270 samples are split into training and validation sets in a 9: 1 ratio, utilizing the standard test set configuration. For TCGA-NSCLC, 1053 WSIs subtypes are split into training, validation, and test sets at ratios of 60: 15: 25, respectively. CDFA-MIL framework is trained using the Adam optimizer with a learning rate of $3e-4$ (cosine decay) and a weight decay of $3e-5$ across 80 epochs. Cross entropy loss is used as a loss function for training and validation. Experiments are facilitated using NVIDIA GeForce RTX 4090 and RTX 3090 GPUs.

4.2 Comparative Analysis and Ablation Study

The CDFA-MIL framework’s performance with diverse magnification combinations excels against benchmark Single-mag and Multi-mag MIL methods. This is evident in our comprehensive results (Tab. 1), showcasing superior ACC, F1, and competitive AUC scores across datasets.

Table 1: Comparison with state-of-the-art methods (mean \pm std), where ‘A.’ denotes ACC, ‘F.’ denotes F1, ‘U.’ denotes AUC. Specifically, in Camelyon-16, CDFA-MIL \dagger correspond to $10\times$ and $20\times$ magnification fusion version, CDFA-MIL \ddagger for $20\times$ and $40\times$, CDFA-MIL for $10\times$ and $40\times$. In TCGA-NSCLC, these are $5\times$ and $10\times$, $10\times$ and $20\times$, $5\times$ and $20\times$.

Method	Paper	Camelyon-16			TCGA-NSCLC		
		A.(%)	F.(%)	U.(%)	A.(%)	F.(%)	U.(%)
CLAM-SB [20]	NBE’21	83.7 \pm 1.7	77.5 \pm 1.4	87.1 \pm 2.6	82.4 \pm 1.6	83.1 \pm 1.0	90.2 \pm 1.2
CLAM-MB [20]	NBE’21	82.3 \pm 1.9	77.4 \pm 2.7	87.8 \pm 4.2	81.8 \pm 1.5	80.6 \pm 4.2	90.1 \pm 3.1
AB-MIL [12]	ICML’18	83.5 \pm 3.5	82.7 \pm 2.4	81.7 \pm 4.9	84.9 \pm 4.1	84.8 \pm 3.9	86.8 \pm 2.8
DTFD-MIL [44]	CVPR’22	88.2 \pm 1.1	84.9 \pm 0.8	93.2 \pm 1.7	87.1 \pm 3.2	86.6 \pm 4.2	92.7 \pm 4.2
DSMIL [14]	CVPR’21	89.9 \pm 6.3	81.5 \pm 2.3	91.6 \pm 5.5	87.5 \pm 4.4	88.6 \pm 5.4	90.0 \pm 3.9
TransMIL [29]	NIPS’21	88.3 \pm 0.5	79.7 \pm 1.7	93.0 \pm 1.0	87.1 \pm 0.3	86.4 \pm 2.0	92.5 \pm 2.1
Zoommil [34]	ECCV’22	84.2 \pm 4.8	83.3 \pm 6.2	79.8 \pm 7.5	86.3 \pm 4.1	85.3 \pm 5.3	85.3 \pm 6.9
HIPT [3]	CVPR’22	89.0 \pm 0.8	-	95.1 \pm 1.9	87.8 \pm 1.3	-	97.7 \pm 2.1
DSMIL-LC [14]	CVPR’21	89.9 \pm 5.7	-	91.6 \pm 5.9	82.9 \pm 6.4	84.4 \pm 7.9	90.4 \pm 4.2
HAG-MIL [41]	arXiv’23	89.3 \pm 2.4	86.9 \pm 2.6	93.7 \pm 1.5	85.7 \pm 1.3	85.3 \pm 1.3	91.5 \pm 0.9
CDFA-MIL \dagger	Ours	87.6 \pm 2.2	87.1 \pm 2.3	84.1 \pm 4.1	92.8 \pm 1.7	93.6 \pm 2.8	92.8 \pm 1.5
CDFA-MIL \ddagger	Ours	92.2 \pm 3.6	91.1 \pm 3.2	90.2 \pm 2.5	91.3 \pm 2.5	92.6 \pm 2.6	91.2 \pm 3.0
CDFA-MIL	Ours	94.6 \pm 1.4	94.5 \pm 1.3	93.7 \pm 1.7	90.6 \pm 1.6	92.0 \pm 3.4	90.8 \pm 1.9

Comparison with the State-of-the-art Methods. The common magnifications used in recent years for multi-mag MIL methods are followed to ensure that consistent magnification appear in the comparison model [3, 10, 14, 32, 34, 41]. In

Camelyon-16, we chose $10\times$, $20\times$ and $40\times$ for two-by-two combinations, and in TCGA-NSCLC, we chose $5\times$, $10\times$ and $20\times$ for two-by-two combinations.

In the Camelyon-16, characterized by minimal cancerous regions averaging less than 10%, the performance of the CDFA-MIL with different combinations of magnifications indicated that the combination of $10\times$ and $20\times$ magnifications had the lowest performance, but it still performed within the top tier of existing MIL methods. The optimal combination of $10\times$ and $40\times$ magnifications in the CDFA-MIL achieved ACC, F1, and AUC values of 94.6%, 94.5%, and 93.7%, respectively, significantly outperforming other methods. For example, the ACC of the combination of $10\times$ and $40\times$ magnifications was 4.7% higher than the second-best MIL method, and the F1 was 7.6% higher.

In the TCGA-NSCLC, with larger tumor regions, MIL methods generally fared well. Our CDFA-MIL[†] with $5\times$ and $10\times$ magnifications achieved the highest ACC and F1 (92.8% and 93.6%) and a competitive AUC (92.8%), surpassing other methods. Specifically, the ACC was higher than the second-best method by 4.3%, and the F1 was 5.0% higher.

These results underscore CDFA-MIL’s efficacy, particularly noting that optimal magnification combinations varied: $10\times$ and $40\times$ in Camelyon-16 and $5\times$ and $10\times$ in TCGA-NSCLC. This discrepancy likely stems from Camelyon-16’s smaller cancerous regions, necessitating $40\times$ magnification for minute lesion observation, in contrast to TCGA-NSCLC’s larger lesions, where high magnification could lead to information loss. Thus, adapting magnification combinations to tumor size is a crucial consideration.

Further Ablation Experiments. Our ablation experiments incorporated point-to-area feature-column attention (PTA) and point-to-point concentric-row attention (PTP) within the AB-MIL framework at high magnification. These adaptations, PTA and PTP, were evaluated on Camelyon-16 and TCGA-NSCLC datasets, assessing accuracy, F1-score, and AUC. Further, T-SNE visualizations elucidated PTA’s clustering efficacy, gauged by v-score and silhouette-score. We also employed information entropy and correlation analysis to ascertain PTA and PTP’s capability in augmenting feature representation and diminishing information redundancy. The subsequent sections detail these experimental proceedings.

In the Camelyon-16 and TCGA-NSCLC datasets classification (Tab. 2), PTA excelled over AB-MIL, enhancing ACC, F1, and AUC by 4.4%, 4.7%, and 4.9%. Following [15], T-SNE analyses (Fig. 5) demonstrated PTA’s improved inter-class differentiation and intra-class consistency, with v-score and silhouette-score increasing by 40.25% and 17.10% over AB-MIL.

For a quantitative evaluation of feature representation, we applied the concept of information entropy to gauge the informational content of patch features, with findings presented in Fig. 6 (A). Notably, the attention-focused patch features in PTA contained considerably more information than those extracted by the baseline model, especially in the TCGA-NSCLC, where information entropy saw a near 40-bit increase. These results underscore PTA’s effective utilization of channel-based attention allocation to bridge the domain gap and augment feature representation, underscoring its practicality and effectiveness. In clas-

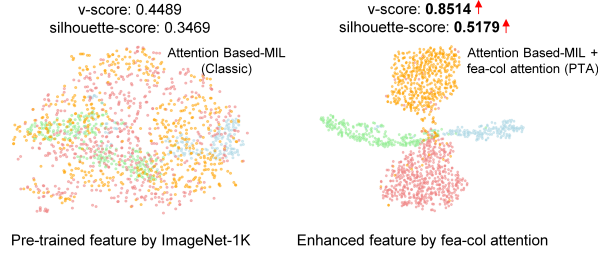


Fig. 5: T-SNE visualization and cluster evaluation measurements of different representations ability: The feature-column attention converts chaotic ImageNet-1K features (left) into more separable distributions (right). The T-SNE visualizations and cluster evaluation measures, v-scores and silhouette-scores, show that enhanced features have higher inter-class separation and intra-class clustering.

Table 2: The result on the ablation experiments: The feature-column attention and concentric-row attention were incorporated into AB-MIL, referred to as PTA and PTP respectively, and their performance was evaluated on two datasets.

Method	Camelyon-16			TCGA-NSCLC		
	A.(%)	F.(%)	U.(%)	A.(%)	F.(%)	U.(%)
AB-MIL (Classic)	84.5	84.0	81.2	85.3	85.2	86.3
PTA (Fea-col attn)	89.2	89.1	87.7	89.4	89.4	89.5
PTP (Con-row attn)	88.4	87.8	84.7	87.9	87.9	87.7

sification tasks on Camelyon-16 and TCGA-NSCLC datasets (Tab. 2), PTP consistently outperformed AB-MIL under controlled external variables, showing average improvements of 3.3% in both ACC and F1, and 2.5% in AUC. Additionally, we utilized cosine similarity and correlation coefficients to analyze patch relationships across magnifications, with findings presented in Fig. 6 (B). The registered indices of global fusion (GF) revealed a significant amalgamation of unrelated information in different magnifications. Conversely, PTP fusion manifested indices 10% and 7% higher than GF, credited to our strategic fusion of highly correlated areas in point-to-point concentric patch, thereby efficiently mitigating the infusion of redundant information and enhancing the discernment of key patches.

4.3 Visualisation of the Concentric Dual Fusion Attention Scores

We demonstrated our model’s interpretability by using concentric dual fusion attention scores for heatmap visualizations on the Camelyon-16 dataset with patch-level annotations. Tumors in the original images are outlined in blue, while heatmaps highlight high-attention areas in red. As shown in Fig. 7, our

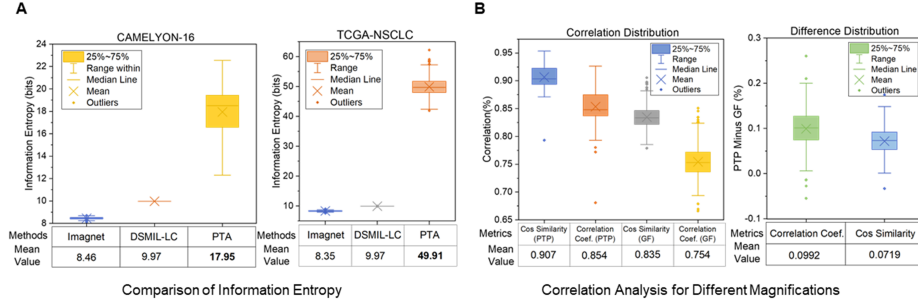


Fig. 6: Visualization of model and fusion method effectiveness: (A) Comparing the information quantity of features extracted by pre-trained model (ImageNet-1K), self-supervised fine-tuning (DSMIL-LC), and point-to-area feature-column attention weighted enhancement (PTA). (B) Point-to-point (PTP) and global fusion (GF) method comparison based on cosine similarity (Cos.) and correlation coefficient (Coef.).

CDFA-MIL effectively identifies key cancer regions, closely matching pathologist annotations, though it is less effective with small, dispersed tumors.

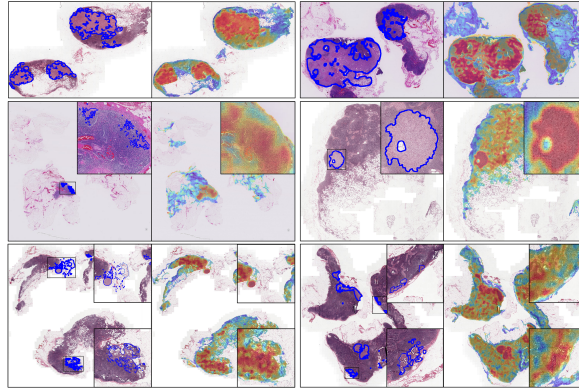


Fig. 7: CDFA-MIL heatmap in Camelyon-16: Pathologists' annotations (left) and the model-generated heatmap (right) highlight differences between expert evaluations and algorithmic detections.

5 Conclusion

In our study, we introduce the Concentric Dual Fusion Attention-MIL (CDFA-MIL), an advanced framework for weakly supervised classification of Whole Slide Images (WSIs). CDFA-MIL effectively overcomes challenges in fusing correlated

information, addressing issues like inadequate feature representation and the excessive inclusion of distant patches in the fusion process. Our approach begins by delineating highly correlated regions through completed concentric patches for each high-magnification patch. We then employ point-to-area feature-column attention, based on channel correlation modeling, to assign weights to feature points, enhancing the representational capacity of features across domain gaps. Additionally, we incorporate a point-to-point concentric-row attention mechanism, targeting these correlated regions, to refine the fusion process and focus on relevant patches.

References

1. Bejnordi, B.E., Veta, M., Van Diest, P.J., Van Ginneken, B., Karssemeijer, N., Litjens, G., Van Der Laak, J.A., Hermsen, M., Manson, Q.F., Balkenhol, M., et al.: Diagnostic assessment of deep learning algorithms for detection of lymph node metastases in women with breast cancer. *Jama* **318**(22), 2199–2210 (2017) [10](#)
2. Campanella, G., Hanna, M.G., Geneslaw, L., Mirafior, A., Werneck Krauss Silva, V., Busam, K.J., Brogi, E., Reuter, V.E., Klimstra, D.S., Fuchs, T.J.: Clinical-grade computational pathology using weakly supervised deep learning on whole slide images. *Nature medicine* **25**(8), 1301–1309 (2019) [2](#), [4](#), [5](#)
3. Chen, R.J., Chen, C., Li, Y., Chen, T.Y., Trister, A.D., Krishnan, R.G., Mahmood, F.: Scaling vision transformers to gigapixel images via hierarchical self-supervised learning. In: *CVPR*. pp. 16144–16155 (2022) [2](#), [4](#), [5](#), [11](#)
4. Cheng, S., Liu, S., Yu, J., Rao, G., Xiao, Y., Han, W., Zhu, W., Lv, X., Li, N., Cai, J., et al.: Robust whole slide image analysis for cervical cancer screening using deep learning. *Nature communications* **12**(1), 5639 (2021) [2](#)
5. Dehaene, O., Camara, A., Moindrot, O., de Lavergne, A., Courtiol, P.: Self-supervision closes the gap between weak and strong supervision in histology. *arXiv preprint arXiv:2012.03583* (2020) [2](#), [4](#)
6. Deng, J., Dong, W., Socher, R., Li, L.J., Li, K., Fei-Fei, L.: Imagenet: A large-scale hierarchical image database. In: *CVPR*. pp. 248–255 (2009) [2](#), [5](#)
7. Hashimoto, N., Fukushima, D., Koga, R., Takagi, Y., Ko, K., Kohno, K., Nakaguro, M., Nakamura, S., Hontani, H., Takeuchi, I.: Multi-scale domain-adversarial multiple-instance cnn for cancer subtype classification with unannotated histopathological images. In: *CVPR*. pp. 3852–3861 (2020) [2](#), [4](#)
8. He, K., Zhang, X., Ren, S., Sun, J.: Deep residual learning for image recognition. In: *CVPR*. pp. 770–778 (2016) [5](#), [6](#)
9. Hou, L., Samaras, D., Kurc, T.M., Gao, Y., Davis, J.E., Saltz, J.H.: Patch-based convolutional neural network for whole slide tissue image classification. In: *CVPR*. pp. 2424–2433 (2016) [1](#), [4](#)
10. Hou, W., Yu, L., Lin, C., Huang, H., Yu, R., Qin, J., Wang, L.: H^2 -mil: Exploring hierarchical representation with heterogeneous multiple instance learning for whole slide image analysis. In: *AAAI*. pp. 933–941 (2022) [2](#), [4](#), [11](#)
11. Hu, J., Shen, L., Sun, G.: Squeeze-and-excitation networks. In: *CVPR*. pp. 7132–7141 (2018) [3](#), [4](#), [8](#)
12. Ilse, M., Tomczak, J., Welling, M.: Attention-based deep multiple instance learning. In: *International conference on machine learning*. pp. 2127–2136 (2018) [2](#), [3](#), [4](#), [5](#), [11](#)
13. Lee, Y., Park, J.H., Oh, S., Shin, K., Sun, J., Jung, M., Lee, C., Kim, H., Chung, J.H., Moon, K.C., et al.: Derivation of prognostic contextual histopathological features from whole-slide images of tumours via graph deep learning. *Nature Biomedical Engineering* pp. 1–15 (2022) [1](#), [2](#)
14. Li, B., Li, Y., Eliceiri, K.W.: Dual-stream multiple instance learning network for whole slide image classification with self-supervised contrastive learning. In: *CVPR*. pp. 14318–14328 (2021) [2](#), [4](#), [11](#)
15. Li, H., Zhu, C., Zhang, Y., Sun, Y., Shui, Z., Kuang, W., Zheng, S., Yang, L.: Task-specific fine-tuning via variational information bottleneck for weakly-supervised pathology whole slide image classification. In: *CVPR*. pp. 7454–7463 (2023) [2](#), [4](#), [12](#)

16. Li, R., Yao, J., Zhu, X., Li, Y., Huang, J.: Graph cnn for survival analysis on whole slide pathological images. In: International Conference on Medical Image Computing and Computer-Assisted Intervention (MICCAI). pp. 174–182 (2018) [2](#)
17. Lin, J., Han, G., Pan, X., Liu, Z., Chen, H., Li, D., Jia, X., Shi, Z., Wang, Z., Cui, Y., et al.: Pdbl: Improving histopathological tissue classification with plug-and-play pyramidal deep-broad learning. *IEEE Transactions on Medical Imaging* **41**(9), 2252–2262 (2022) [2](#)
18. Lin, T., Yu, Z., Hu, H., Xu, Y., Chen, C.W.: Interventional bag multi-instance learning on whole-slide pathological images. In: CVPR. pp. 19830–19839 (2023) [1](#), [4](#)
19. Liu, Z., Lin, Y., Cao, Y., Hu, H., Wei, Y., Zhang, Z., Lin, S., Guo, B.: Swin transformer: Hierarchical vision transformer using shifted windows. In: ICCV. pp. 10012–10022 (2021) [5](#)
20. Lu, M.Y., Williamson, D.F., Chen, T.Y., Chen, R.J., Barbieri, M., Mahmood, F.: Data-efficient and weakly supervised computational pathology on whole-slide images. *Nature biomedical engineering* **5**(6), 555–570 (2021) [1](#), [2](#), [3](#), [5](#), [7](#), [10](#), [11](#)
21. Maron, O., Lozano-Pérez, T.: A framework for multiple-instance learning. In: Advances in Neural Information Processing Systems. p. 570–576 (1997) [2](#), [4](#)
22. Mobadersany, P., Yousefi, S., Amgad, M., Gutman, D.A., Barnholtz-Sloan, J.S., Velázquez Vega, J.E., Brat, D.J., Cooper, L.A.: Predicting cancer outcomes from histology and genomics using convolutional networks. *Proceedings of the National Academy of Sciences* **115**(13), E2970–E2979 (2018) [2](#)
23. Muhammad, H., Sigel, C.S., Campanella, G., Boerner, T., Pak, L.M., Büttner, S., IJzermans, J.N., Koerkamp, B.G., Doukas, M., Jarnagin, W.R., et al.: Unsupervised subtyping of cholangiocarcinoma using a deep clustering convolutional autoencoder. In: Medical Image Computing and Computer Assisted Intervention–MICCAI 2019: 22nd International Conference, Shenzhen, China, October 13–17, 2019, Proceedings, Part I 22. pp. 604–612 (2019) [2](#)
24. Pinckaers, H., Van Ginneken, B., Litjens, G.: Streaming convolutional neural networks for end-to-end learning with multi-megapixel images. *IEEE TPAMI* **44**(3), 1581–1590 (2020) [4](#)
25. Pleasure, M., Redekop, E., Polson, J.S., Zhang, H., Kaneko, N., Speier, W., Arnold, C.W.: Pathology-based ischemic stroke etiology classification via clot composition guided multiple instance learning. In: ICCV. pp. 2674–2683 (2023) [4](#)
26. Qu, L., Yang, Z., Duan, M., Ma, Y., Wang, S., Wang, M., Song, Z.: Boosting whole slide image classification from the perspectives of distribution, correlation and magnification. In: ICCV. pp. 21463–21473 (2023) [2](#), [4](#)
27. de Santana Correia, A., Colombini, E.L.: Attention, please! a survey of neural attention models in deep learning. *Artificial Intelligence Review* **55**(8), 6037–6124 (2022) [5](#)
28. Schmitz, R., Madesta, F., Nielsen, M., Krause, J., Steurer, S., Werner, R., Rösch, T.: Multi-scale fully convolutional neural networks for histopathology image segmentation: from nuclear aberrations to the global tissue architecture. *Medical image analysis* **70**, 101996 (2021) [4](#)
29. Shao, Z., Bian, H., Chen, Y., Wang, Y., Zhang, J., Ji, X., zhang, y.: Transmil: Transformer based correlated multiple instance learning for whole slide image classification. pp. 2136–2147 (2021) [4](#), [5](#), [11](#)
30. Shats, D., Hezi, H., Shani, G., Maruvka, Y.E., Freiman, M.: Patient-level microsatellite stability assessment from whole slide images by combining momentum contrast learning and group patch embeddings. In: ECCV. pp. 454–465 (2022) [2](#), [4](#)

31. Shi, J., Tang, L., Li, Y., Zhang, X., Gao, Z., Zheng, Y., Wang, C., Gong, T., Li, C.: A structure-aware hierarchical graph-based multiple instance learning framework for pt staging in histopathological image. *IEEE Transactions on Medical Imaging* **42**(10), 3000–3011 (2023) [2](#)
32. Srinidhi, C.L., Ciga, O., Martel, A.L.: Deep neural network models for computational histopathology: A survey. *Medical Image Analysis* **67**, 101813 (2021) [2](#), [3](#), [4](#), [11](#)
33. Srinidhi, C.L., Kim, S.W., Chen, F.D., Martel, A.L.: Self-supervised driven consistency training for annotation efficient histopathology image analysis. *Medical Image Analysis* **75**, 102256 (2022) [4](#)
34. Thandiackal, K., Chen, B., Pati, P., Jaume, G., Williamson, D.F., Gabrani, M., Goksel, O.: Differentiable zooming for multiple instance learning on whole-slide images. In: *ECCV*. pp. 699–715 (2022) [2](#), [3](#), [4](#), [5](#), [11](#)
35. Tomczak, K., Czerwińska, P., Wiznerowicz, M.: Review the cancer genome atlas (tcga): an immeasurable source of knowledge. *Contemporary Oncology/Współczesna Onkologia* **2015**(1), 68–77 (2015) [10](#)
36. TU, C., ZHANG, Y., Ning, Z.: Dual-curriculum contrastive multi-instance learning for cancer prognosis analysis with whole slide images. pp. 29484–29497 (2022) [2](#)
37. Van Rijnthoven, M., Balkenhol, M., Siliņa, K., Van Der Laak, J., Ciompi, F.: Hooknet: Multi-resolution convolutional neural networks for semantic segmentation in histopathology whole-slide images. *Medical image analysis* **68**, 101890 (2021) [4](#)
38. Wang, X., Xiang, J., Zhang, J., Yang, S., Yang, Z., Wang, M.H., Zhang, J., Yang, W., Huang, J., Han, X.: Scl-wc: Cross-slide contrastive learning for weakly-supervised whole-slide image classification. pp. 18009–18021 (2022) [2](#), [4](#)
39. Wibawa, M.S., Lo, K.W., Young, L.S., Rajpoot, N.: Multi-scale attention-based multiple instance learning for classification of multi-gigapixel histology images. In: *ECCV*. pp. 635–647 (2022) [2](#), [3](#), [4](#), [5](#)
40. Xiang, H., Shen, J., Yan, Q., Xu, M., Shi, X., Zhu, X.: Multi-scale representation based deep multiple instance learning for gigapixel whole slide image analysis. *Medical Image Analysis* **89**, 102890 (2023) [2](#), [4](#), [5](#)
41. Xiong, C., Chen, H., Sung, J., King, I.: Diagnose like a pathologist: Transformer-enabled hierarchical attention-guided multiple instance learning for whole slide image classification. *arXiv preprint arXiv:2301.08125* (2023) [11](#)
42. Yao, J., Zhu, X., Jonnagaddala, J., Hawkins, N., Huang, J.: Whole slide images based cancer survival prediction using attention guided deep multiple instance learning networks. *Medical Image Analysis* **65**, 101789 (2020) [2](#), [5](#)
43. Yu, K.H., Zhang, C., Berry, G.J., Altman, R.B., Ré, C., Rubin, D.L., Snyder, M.: Predicting non-small cell lung cancer prognosis by fully automated microscopic pathology image features. *Nature communications* **7**(1), 12474 (2016) [1](#)
44. Zhang, H., Meng, Y., Zhao, Y., Qiao, Y., Yang, X., Coupland, S.E., Zheng, Y.: Dtf-d-mil: Double-tier feature distillation multiple instance learning for histopathology whole slide image classification. In: *CVPR*. pp. 18802–18812 (2022) [2](#), [4](#), [11](#)
45. Zhou, J., Wang, X., Wei, Z., Meng, J., Huang, D.: 4accpred: Weakly supervised prediction of n4-acetyldeoxycytosine dna modification from sequences. *Molecular Therapy-Nucleic Acids* **30**, 337–345 (2022) [4](#)
46. Zhu, X., Yao, J., Zhu, F., Huang, J.: Wsisa: Making survival prediction from whole slide histopathological images. In: *CVPR*. pp. 7234–7242 (2017) [1](#), [2](#)